



# Ultrathin $\text{ZnIn}_2\text{S}_4/\text{ZnSe}$ heteronanosheets with modulated S-scheme enable high efficiency of visible-light-responsive photocatalytic hydrogen evolution

Yueqi Zhong, Mengyuan Li, Xue Luan, Fangfang Gao, Hanxiang Wu, Jiangzhi Zi, Zichao Lian<sup>\*</sup>

School of Materials and Chemistry, University of Shanghai for Science and Technology, Shanghai 200093, PR China

## ARTICLE INFO

### Keywords:

Heterojunction photocatalysts  
Photocatalytic water splitting for  $\text{H}_2$   
 $\text{ZnIn}_2\text{S}_4/\text{ZnSe}$  heteronanosheets  
S-scheme mechanism

## ABSTRACT

The photoinduced carrier transfer mechanism in heterojunction photocatalysts plays a significant role in photocatalytic water splitting. However, the relationships between photocatalytic activity and different band alignments in semiconducting heteronanosheets (HNSs) are rarely reported. Here, we used the ultrathin  $\text{ZnIn}_2\text{S}_4$  (ZIS) as a model, and constructed the HNSs such as  $\text{ZIS}/\text{ZnSe}$ ,  $\text{ZIS}/\text{ZnS}$  with different band alignments. The time-resolved transient absorption results show that  $\text{ZIS}/\text{ZnSe}$  HNSs exhibited the S-scheme mechanism forming the internal electronic field which has more advantages in HER than the defects state trapping-mediated transfer mechanism in  $\text{ZIS}/\text{ZnS}$  HNSs. The long-lived carrier separation ( $>3.58 \mu\text{s}$ ) and efficient charge transfer pathways of  $\text{ZIS}/\text{ZnSe}$  HNSs contribute to a highest photocatalytic performance so far, compared with the ZIS-based photocatalysts. These results could pave the route for the design the functional HNCs with different photoinduced carrier dynamics to establish the relationships between composite structures and properties.

## 1. Introduction

Hydrogen as a sustainable energy with high energy density, has the advantage of mitigating energy crisis to sustain global population and economic growth. Therefore, it could be considered as an excellent candidate to replace the fossil fuel [1–4]. Photocatalytic water splitting to hydrogen can skillfully convert sustainable solar energy to  $\text{H}_2$  energy through semiconductor photocatalysts, without emitting any pollutants during the whole process, in accordance with the current goal of carbon neutralization and conforming to the sustainable development concept [5,6]. However, low conversion efficiency for photocatalytic hydrogen evolution has become a heavily obstacle due to the rapid recombination of the unexpected photoinduced electron-hole pairs in the hydrogen evolution reactions (HER). Therefore, it is urgent to rationally design and construct heterostructured nanocrystals (HNCs) with multifunctional properties to alleviate this unnecessary carrier recombination process and improve the photocatalytic efficiency of hydrogen evolution [7–10].

Recently, metal polysulfide semiconductor photocatalysts, such as  $\text{CdS}$ ,  $\text{CuInS}_2$ , and  $\text{ZnIn}_2\text{S}_4$  (ZIS) etc., have attracted much attention due to their excellent visible light response ability [11,12]. Particularly, ZIS is a promising layered transition metal chalcogenide with a tunable band

gap of 2.06 ~ 2.85 eV and a conduction band of about - 1.20 eV, indicating that photogenerated electrons have strong reducing ability and suitable for photocatalytic HER [13]. Besides, due to its unique layered structure, remarkable photostability, and environmental friendliness, it has attracted more attentions of researchers [14]. Whereas, the photocatalytic activity in HER of the single ZIS is not satisfactory in practical application due to the unexpected photo-generated electron-hole pair recombination [15]. To realize the high performance in HER, the construction of heterostructures with an efficient charge transfer pathways could give a way for achieving the multifunction in each phase. Especially, zinc selenide ( $\text{ZnSe}$ ) is a stable and cheap semiconductor with a strong visible light absorption capacity due to its suitable band gap (2.8 eV), no toxicity, and its appropriate conduction band (CB) which could provide sufficient driving force for the decomposition and reduction of water to produce hydrogen [16,17]. Generally, the heterostructured semiconductor NCs with suitable band-gaps can be synthesized around nanoparticles to construct an internal electric field by taking advantages of the difference in band structure between them, thus limiting the recombination of photo-generated carriers and effectively improving the chemical stability of colloidal nanomaterials. In addition, the internal electric field at the materials interface between heterostructured NCs can also promote the

<sup>\*</sup> Corresponding author.

E-mail address: [zichaolian@usst.edu.cn](mailto:zichaolian@usst.edu.cn) (Z. Lian).

<https://doi.org/10.1016/j.apcatb.2023.122859>

Received 28 January 2023; Received in revised form 20 April 2023; Accepted 5 May 2023

Available online 6 May 2023

0926-3373/© 2023 Elsevier B.V. All rights reserved.

effective separation of photogenerated carrier, further improving the photocatalytic activity [18]. As the researchers proposed the S-scheme charge transfer in HNCs—under the influence of the internal electric field, the photogenerated electrons in the conduction band of a semiconductor with lower Fermi level can be directionally transferred to the valence band of another semiconductor with higher Fermi level—could realize the chemical potentials in each for enhanced the photocatalytic activity in HER [19–22]. Therefore, the rational design of the S-scheme in HNCs could achieve the superior photocatalytic activity in HER.

Herein, we successfully synthesized ultrathin ZIS/ZnSe hetero-nanosheets (HNSs) with a unique sunflower structure, which shows the S-scheme charge separation. The ZIS/ZnSe HNSs exhibited higher photocatalytic activity in HER ( $1296.9 \mu\text{mol h}^{-1} \text{g}^{-1}$ ) under visible light irradiation, which was 2.47 and 6.34 times that of ZIS/ZnS HNSs ( $525.2 \mu\text{mol h}^{-1} \text{g}^{-1}$ ) and ZIS NSs ( $204.4 \mu\text{mol h}^{-1} \text{g}^{-1}$ ), respectively. In addition, the apparent quantum yield (AQY) of 1 wt% Pt-ZIS/ZnSe HNSs could reach 10.9% at 420 nm with the hydrogen production rate was  $3332.2 \mu\text{mol h}^{-1} \text{g}^{-1}$ , which is the highest activity in HER compared with ZIS-based HNCs so far, as shown in Table S1. The high photocatalytic activity could be attributed to the long lifetime of the photoinduced charge separation in ZIS/ZnS HNSs as revealed by the transient absorption measurements. Moreover, it could be found that the S-scheme charge transfer is more effective than the charge separation of the defect-mediated electron trapped pathway, which paved the route for further determination of the relationships between the photocatalytic activity and photoinduced carrier transfer pathways.

## 2. Experimental section

### 2.1. Materials

#### 2.1.1. Synthesis of $\text{ZnIn}_2\text{S}_4$ nanosheets

A mixture of  $\text{ZnCl}_2$  (1 mmol),  $\text{InCl}_3 \cdot 4 \text{H}_2\text{O}$  (2 mmol) and oleylamine (20 mL) was degassed at  $70^\circ\text{C}$  for 40 min, heated to  $120^\circ\text{C}$ . It was degassed for 20 min and heated at  $180^\circ\text{C}$  under a nitrogen atmosphere. The mixture of 1-dodecanethiol and tert-dodecyl mercaptan (total 7.5 mL, v-v=1:10) was swiftly injected to the above solution. Then the solution was rapidly increased the temperature to  $240^\circ\text{C}$  and kept it for 10 min (including heating time). After the reaction, the resulting products were purified with a mixed solution of hexane and ethanol, centrifuged twice, and re-dispersed in hexane for further characterizations.

#### 2.1.2. Synthesis of ZIS/ZnSe HNSs

A mixture of zinc acetate (1.8 mmol), oleic acid (2 mL), and 1-octadecene (6 mL) was degassed at  $150^\circ\text{C}$  for 30 min in a three-necked flask. Then it was heated to  $250^\circ\text{C}$  for 1 h under a nitrogen atmosphere and cooled to  $70^\circ\text{C}$ . Then, the ZIS NSs hexane solution (1 mL, 0.02 M) was swiftly injected into the solution and degassed for 30 min, followed by heating to  $250^\circ\text{C}$ . A mixture of Se (0.9 mmol) and trioctylphosphine (2 mL) was added to the above solution at the rate of  $0.1 \text{ mL min}^{-1}$ . After finishing the injection process, the reaction was allowed to proceed for a further 40 min. The solution was then cooled to room temperature, and purified with a mixed solution of chloroform and ethanol, centrifuged twice, and dispersed in chloroform for further characterizations.

#### 2.1.3. Synthesis of ZIS/ZnS HNSs

A mixture of zinc acetate (1.8 mmol), oleic acid (2 mL), and 1-octadecene (6 mL) was degassed at  $150^\circ\text{C}$  for 30 min in a three-necked flask. Then it was heated to  $250^\circ\text{C}$  and kept it for 1 h under an atmosphere of nitrogen. The solution was cooled to  $70^\circ\text{C}$ , at which point 1 mL of 0.02 M ZIS NSs hexane solution was swiftly injected. The mixture solution was degassed for 30 min and heated to  $250^\circ\text{C}$ . A trioctylphosphine (2 mL) solution of S (0.9 mmol) was then added to the above solution at a rate of  $0.1 \text{ mL min}^{-1}$ . After the injection process, the reaction was allowed to proceed for a further 40 min. The solution was then cooled to

room temperature, washed twice with a mixed solvent of chloroform and ethanol, then centrifuged, and dispersed in chloroform for further characterization.

#### 2.1.4. Preparation of water-soluble samples

The synthesized photocatalysts were transferred from a chloroform phase to an aqueous phase using the formamide and  $(\text{NH}_4)_2\text{S}$ -assisted phase transfer method. After 10 mL of chloroform containing 20 mg of photocatalysts were added to a 30 mL glass bottle, a mixture of the 9.5 mL formamide and 0.5 mL  $(\text{NH}_4)_2\text{S}$  aqueous solution was added into the above solution under vigorous stirring. After 2 h, the resulting samples were transferred to the aqueous phase by the ligand exchange. The  $\text{S}^{2-}$ -capped photocatalysts were collected by centrifugation with ethanol. Finally, the as-obtained samples were dried under vacuum for further characterization.

### 2.2. Characterization

Transmission electron microscopy (TEM) was performed on a HT7800 (Hitachi) operating an acceleration voltage of 120 kV. High-resolution TEM (HRTEM) was carried out on a Talos F200X (FEI) electron microscope at an acceleration voltage of 200 kV. X-ray diffraction (XRD) measurements were measured using a D/MAX-2000 with  $\text{Cu K}\alpha$  radiation ( $\lambda = 1.5406 \text{ \AA}$ ) at 40 kV and 30 mA. The optical absorbance measurements of all samples were performed using a Shimadzu UV-1900i spectrophotometer. X-ray photoelectron spectroscopy (XPS) measurements was carried out on a Thermo K-Alpha spectrometer with a 300 W Al  $\text{K}\alpha$  radiation source. *In-situ* XPS measurements were performed on a Thermo Scientific Escalab 250Xi with a 150 W Al  $\text{K}\alpha$  radiation at 14.8 kV and 1.6 A, under visible light irradiation ( $\lambda > 420 \text{ nm}$ ). Carbon ( $\text{C } 1 \text{ s} = 284.8 \text{ eV}$ ) was served as a reference for calibrating the binding energies. The ZIS/ZnSe and ZIS/ZnS weight ratio were evaluated via inductively coupled plasma optical emission spectroscopy (ICP-OES, Thermo Fisher iCAP PRO (OES)). Atomic force microscope (AFM) measurement was performed on a Bruker Dimension ICON (Germany). The fluorescence spectrum was recorded on a FLS-1000 steady state fluorescence spectrometer. EPR measurements were taken on a Bruker EMX plus-6/1 spectrometer at room temperature.

### 2.3. Photocatalytic hydrogen evolution

To measure the photocatalytic hydrogen evolution reaction (HER), a GC-2014 (Shimadzu, Kyoto, Japan) was applied to examine the amount of hydrogen evolution by using the nitrogen as the carrier gas. The 5.0 mg samples and 3 mL deionized water with sacrificial agents (0.25 M  $\text{Na}_2\text{S} \cdot 9 \text{H}_2\text{O}$  and 0.35 M  $\text{Na}_2\text{SO}_3$ ) were added to the 25 mL quartz reactor and ultrasonic mixing well for reactions. Then, we evacuated the reactor with the nitrogen cycles several times until the air is totally removed, followed by the irradiation. A 300 W xenon lamp (MAX-303A, BJNBET Technology Co., Ltd.) equipped with a UV cutoff filter ( $\lambda > 420 \text{ nm}$ ) was used as an irradiation light source, and the lamp was placed 4 cm away from the reactor. Under the above photocatalytic reaction conditions, the apparent quantum efficiency (AQY) was measured by a single wavelength 420 nm filter. The intensity of the light was carried out using a photo-radiometer (CEL-NP2000-2). The AQY was calculated according to the following formula:

$$\begin{aligned} \text{AQY} &= \frac{\text{number of reacted electrons}}{\text{number of incident photons}} \times 100\% \\ &= \frac{\text{number of evolved } \text{H}_2 \text{ molecules} \times 2}{\text{number of incident photons}} \times 100\% \end{aligned} \quad (1)$$

### 2.4. Photoelectrochemical (PEC) measurements

The PEC measurements were conducted in a conventional three-electrode system using a single-compartment quartz cell on an

electrochemical station (CHI-660E). The 0.5 M Na<sub>2</sub>SO<sub>4</sub> aqueous solution was used as the electrolyte for PEC measurements. A 150  $\mu$ L solution was used from the mixture of Nafion solution (10  $\mu$ L, 5%), the photocatalyst (3 mg), and ethanol (500  $\mu$ L) and slowly dropped onto FTO conductive glass ( $A = 1 \text{ cm}^2$ ). Then it was dried in the vacuum at 60 °C for 1 h to prepare the working electrodes. A silver chloride electrode (Ag/AgCl) and Pt sheet electrode were used as reference and counter electrodes, respectively. Both the photocurrent and AC impedance measurements were performed at 0.8 V bias voltage and illumination ( $\lambda > 420 \text{ nm}$ ). A 300 W Xe lamp with an ultraviolet (UV) filter ( $\lambda > 420 \text{ nm}$ ) was placed 5 cm away from the photoelectrochemical cell as a visible light source. The open-circuit voltage of the impedance test is in the frequency range of  $10^5 \sim 0.01 \text{ Hz}$  with an AC voltage at  $5 \text{ mV s}^{-1}$ .

## 2.5. Transient absorption (TA) measurements

Transient absorption spectra (TAS) were measured using the femtosecond (fs) transient absorption spectrometer (Helios Fire, Ultrafast System). The samples in chloroform were excited at 300 nm by the Ti:sapphire laser system (Astrella, 800 nm, pulse width, 90 fs, pulse energy, 7 mJ per pulse, repetition rate, 1 kHz, Coherent Inc.). Part of the fundamental (2.0 W of the amplified 800 nm output from the TOPAS, Coherent) was used for a second harmonic BBO crystal to obtain 300 nm as a pump, and the probe pulse was obtained by using amplified 800 nm output (ca. 100 mW) focused on a Ti/Sapphire crystal to generate a white-light continuum over 330–500 nm. The pump and probe beams were focused onto the sample for temporal and spatial overlap. The measurements were performed using chloroform solutions of the as-obtained samples, which were placed in a 1 mm path length quartz cell with stirring at room temperature. The instrument response function of this system was 120 fs.

For the nanosecond to microsecond time-resolved TA measurement, we used the nanosecond TA emission spectrometer designed and made by Dalian Institute of Chemical Physics, which combined with a Nd:YAG nanosecond laser system (Nimma900, Beamtech Optronics Co., Ltd.). Photolysis of the samples was measured with single-flash laser excitation at 355 nm (3 Hz, 9.5 mJ/pulse, full width at half maximum (FWHM)  $\approx 20 \text{ ns}$ ). The analyzing light was from a 450 W pulsed xenon lamp (PL450), a high intensity monochromator (WDG30-Z, Beijing Optical Instrument Factory), and a photomultiplier tube (PMT R928) at the detection end consist of the monitoring system. The transient curve is recorded by digital oscilloscope (Tektronix, MDO3052, analog channel bandwidth 500 M, sampling rate up to 2.5 G/s). Samples with an optical absorbance of 0.6–0.8 in chloroform solution at 370 nm and 640 nm in a 1 mm path length quartz cell were measured. The decay curves were fitted with biexponential functions.

## 3. Results and discussion

### 3.1. Structural Characterization

Firstly, the ZIS/ZnX (X: S, Se) HNSs were synthesized by a seed-mediated heteronucleation growth method using the ZIS NSs as the seeds, as shown in the Fig. 1a, in which the ZIS NSs were the ultrathin hexagonal nanosheets (see Fig. S1 for details) with the thickness of approximately 1.8 nm (details in the Fig. S2). The size of ZIS NSs was determined to be  $60.8 \pm 1.0 \text{ nm}$  (Fig. S3a). Fig. 1b shows the representative transmission electron microscopy (TEM) images of the ZIS/ZnSe HNSs with the morphology of a unique sunflower structure. The size of ZnSe phase in ZIS/ZnSe HNSs was determined to be  $4.9 \pm 0.1 \text{ nm}$  (Fig. S3b). Fig. 1c shows the high-resolution TEM (HRTEM) image of the ZIS/ZnSe HNSs, which revealed the existence of the ZIS and ZnSe phases. The different lattice fringes of 0.32 nm and 0.33 nm (Fig. 1c) corresponded to the *wurtzite*-ZIS (*w*-ZIS) (102) and *w*-ZnSe (002) lattice planes, respectively. Furthermore, the fast Fourier transform (FFT) in Fig. 1d illustrated two different reflection patterns, indicating that the

ZnSe were grown around the ZIS NSs. High-angle annular dark-field (HAADF) scanning TEM (STEM) and STEM-energy dispersive X-ray spectrometry (EDS) mapping (Fig. 1e) showed that the ZIS NSs were covered with ZnSe NPs, which formed a sunflower-like structure. In addition, the ZIS/ZnS HNSs were synthesized using a similar method and its TEM image was shown in Fig. S4a with the morphology of dot-around-sheet structures [23]. The HRTEM image of the ZIS/ZnS HNSs (Fig. S4b) shows the composition of the ZIS NSs and ZnS phase, and the lattice fringe of 0.19 nm corresponds to the *w*-ZnS (110) planes. Fig. S4c shows the HAADF-STEM-EDS elemental mapping of the ZIS/ZnS HNSs, which reflects the uniform dispersion of the elements, and ZnS NPs were mainly distributed around the ZIS NSs with the size of  $3.2 \pm 0.1 \text{ nm}$  (Fig. S3c). The weight ratios of the ZIS/ZnSe and ZIS/ZnS were 1:3.2 and 1:2.6, respectively, as determined by the inductively coupled plasma optical emission spectroscopy (ICP-OES) (see Table S1 for details).

### 3.2. Materials Properties and Photoelectrochemical (PEC) Measurements

The X-ray diffraction (XRD) patterns of ZIS/ZnSe HNSs were shown in Fig. 2a, which reveal that the ZIS/ZnSe HNSs are composed of *wurtzite* ZIS (*w*-ZIS, Joint Committee on Powder Diffraction Standards (JCPDS) no. 65–2023) and *wurtzite* ZnSe (*w*-ZnSe, JCPDS no. 15–0105) phases. In addition, as shown in Fig. S5, the XRD patterns show different amount of ZnSe phases in ZIS/ZnSe HNSs. As the increase of ZnSe phases, we could obviously observe the diffraction peaks of ZnSe phase in ZIS/ZnSe HNSs. As comparison, Fig. 2a gave the XRD pattern of the ZIS/ZnSe HNSs, which was comprising *w*-ZIS and *wurtzite* ZnS (*w*-ZnS, JCPDS no. 36–1405). Fig. 2b shows UV–visible (UV–vis) absorption spectra for the samples, which clearly demonstrate that the hybrid composites exhibit the corresponding features of the characteristic absorption, after ZnS and ZnSe NPs are loaded on the ZIS NSs, respectively. From the absorption spectra of ZIS NSs, ZnS and ZnSe NPs, the band gap energy ( $E_g$ ) could be determined by the following formula:

$$\alpha h\nu = A (h\nu - E_g)^{n/2} \quad (2)$$

where  $\alpha$ ,  $h$ ,  $\nu$ ,  $A$ , and  $E_g$  are absorption coefficients, the Planck constant, light frequency, a constant, and the band gap energy, respectively [24]. The value of the exponent  $n$  is determined by the type of band gap ( $n = 1$  and  $4$  for the direct and indirect band gap, respectively). The values of  $E_g$  for pure ZIS NSs, ZnS NPs and ZnSe NPs were estimated to be about 2.85 eV, 3.60 eV and 2.80 eV (as shown in Fig. S6), respectively, which are consistent with the previous report [25–27]. As shown in Fig. S7, the Mott-Schottky (MS) measurements were performed to determine the Fermi energy levels ( $E_F$ ) of materials [28,29]. The potential vs. RHE was calculated using the following equation:

$$E_{\text{vs-RHE}} = E_{\text{vs-Ag/AgCl}} + 0.1976 + 0.059 \times \text{pH} \quad (3)$$

In general, for an *n*-type semiconductor, the  $E_F$  is about 0–0.2 V more positive than its conduction band (CB) potential [30]. So the potentials of CB for ZIS NSs, ZnS NPs and ZnSe NPs were estimated to be about  $-1.20 \text{ eV}$ ,  $-1.48 \text{ eV}$  and  $-1.05 \text{ eV}$ , respectively. Besides, the corresponding band structures of materials are derived according to the relationships between the valence bands, conduction bands and the band gaps of the materials [31], as shown in the following formula:

$$E_{\text{VB}} = E_{\text{CB}} + E_g \quad (4)$$

Moreover, as shown in Fig. S8, we obtained the energy levels of some vacancies in the ZnS NPs by the fluorescence analysis [32–34]. As shown in Fig. S9, the existence of S vacancies ( $V_S$ ) in ZnS NPs was further proved by the electron paramagnetic resonance (EPR) measurement, the ZnS NPs exhibit a strongly symmetrical EPR signal with  $g = 2.003$  [35, 36]. In addition, the spin number of S vacancies of ZnS NPs were  $1.20 \times 10^{11} \text{ spins mm}^{-3}$ , implying that rich S vacancies are generated in the ZnS NPs. Then, the band energy diagrams for ZIS NS, ZnSe NP, and ZnS NP were illustrated in Fig. S10.



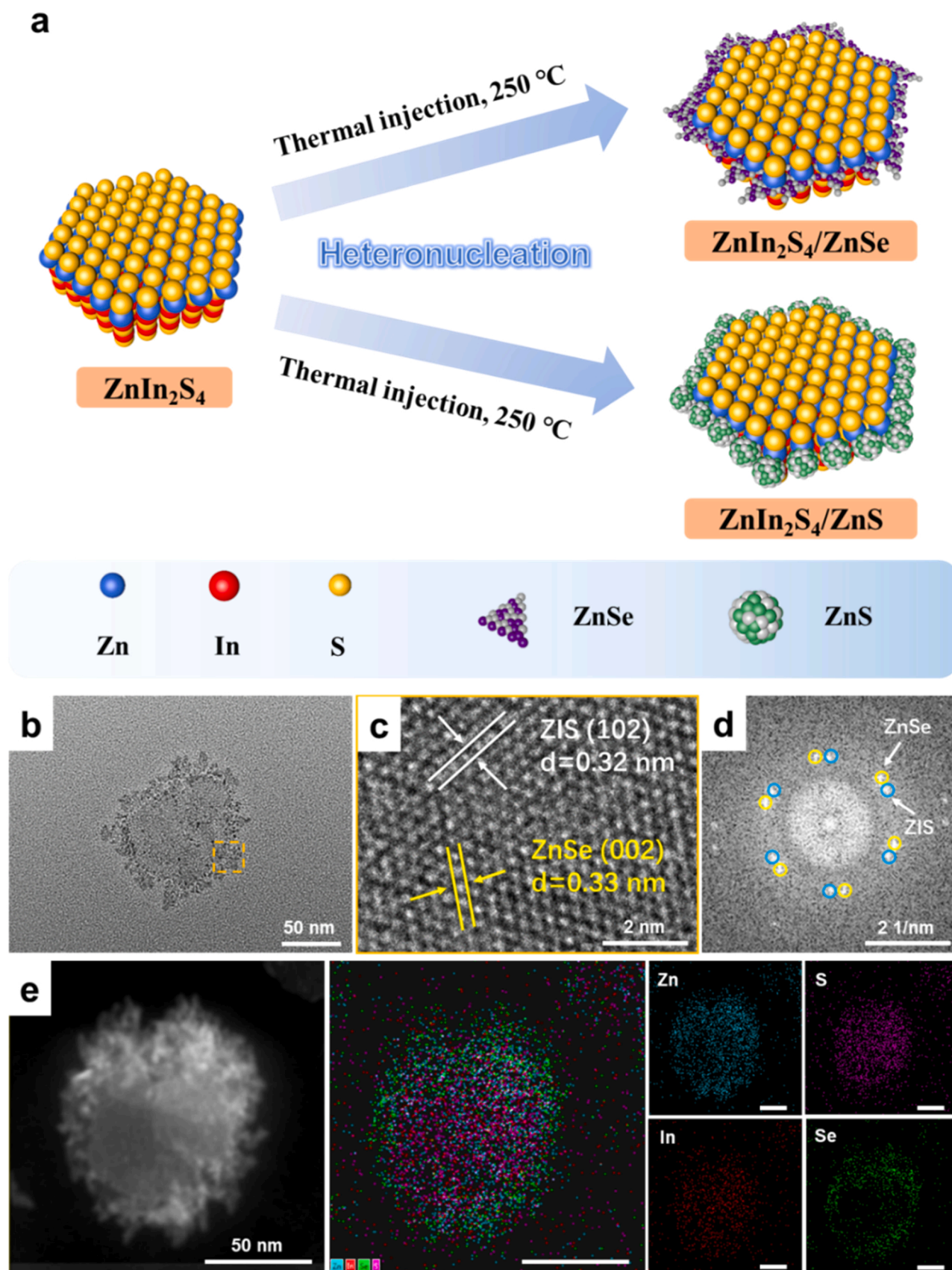


**Fig. 1.** (a) Schematic illustration of the synthetic routes of  $\text{ZnIn}_2\text{S}_4/\text{ZnSe}$  and  $\text{ZnIn}_2\text{S}_4/\text{ZnS}$  heteronanosheets by  $\text{ZnIn}_2\text{S}_4$  nanosheets. (b) Representative TEM image of a single ZIS/ZnSe HNS. (c) HRTEM image of ZIS/ZnSe HNS; Enlargement of the dashed orange rectangle in panel (b). (d) FFT patterns of the orange rectangle (c), where the yellow and blue circle represent the diffraction spots of the  $w$ -ZnSe phase and  $w$ -ZIS phase, respectively. (e) HAADF-STEM-EDS elemental mapping images of a single ZIS/ZnSe HNS; scale bars: 50 nm.

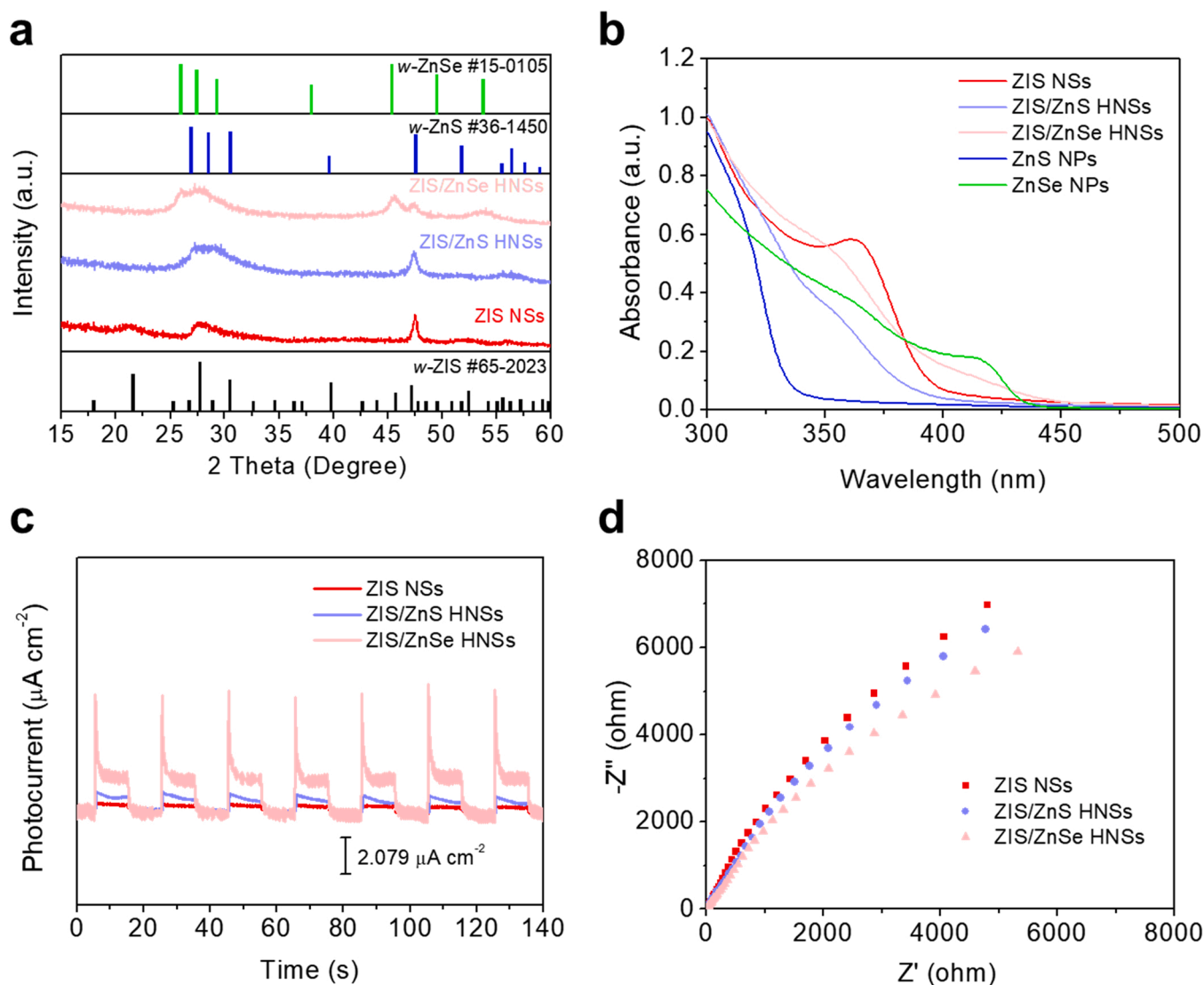


**Fig. 2.** (a) XRD patterns of ZIS NSs, ZIS/ZnS HNSs, and ZIS/ZnSe HNSs. (b) UV-vis spectra of ZIS NSs, ZIS/ZnS HNSs, ZIS/ZnSe HNSs, ZnS NPs, and ZnSe NPs. (c) Photocurrent responses in the light on-off process (0.8 V vs. Ag/AgCl) under visible-light irradiation ( $\lambda > 420$  nm) with 20 s light on/off cycles of ZIS NSs, ZIS/ZnS HNSs, and ZIS/ZnSe HNSs. (d) Nyquist plots of electrochemical impedance spectra of ZIS NSs, ZIS/ZnS HNSs, and ZIS/ZnSe HNSs.

To evaluate the PEC performance of the ZIS/ZnSe HNSs under visible light irradiation ( $\lambda > 420$  nm), we did the transient photocurrent measurements to verify the separation of photoinduced charges. As shown in Fig. 2c, the photocurrent density reveals the charge separation efficiency of ZIS NSs, ZIS/ZnS HNSs, and ZIS/ZnSe HNSs under visible light irradiation. It was noted that ZIS/ZnSe HNSs exhibited a remarkable photocurrent density ( $2.177 \mu\text{A cm}^{-2}$ ), which is 2.77 and 6.05 times higher than those of the ZIS/ZnS HNSs ( $0.785 \mu\text{A cm}^{-2}$ ) and pristine ZIS NSs ( $0.360 \mu\text{A cm}^{-2}$ ), respectively. Furthermore, the electrochemical impedances spectroscopy (EIS) measurements were performed to determine the interfacial properties between the electrode and the electrolyte (Fig. 2d). The results showed that the Nyquist semicircle radius of ZIS/ZnSe HNSs were smaller than that of ZIS/ZnS HNSs and ZIS NSs, indicating that ZIS/ZnSe HNSs have a smaller electron transport impedance and a faster electron mobility [37].

Furthermore, the X-ray photoelectron spectroscopy (XPS) measurements were used to determine the surface valence states of the elements in the photocatalysts, and the in situ XPS measurements can indicate the changes of element binding energy under light irradiation, which can reflect the changes of electron density [38,39]. Meanwhile, the transfer direction of electrons could be known by the variation of binding energy

of elements, which is helpful to further analyze the charge transfer mechanism of materials [40–42]. As shown in Fig. 3a, the peaks at 1022.37 eV (Zn 2p<sub>3/2</sub>) and 1045.43 eV (Zn 2p<sub>1/2</sub>) in ZIS proves the existence of Zn<sup>2+</sup> [43]. The binding energies of 445.10 eV (In 3d<sub>5/2</sub>) and 452.65 eV (In 3d<sub>3/2</sub>) in ZIS were assigned to In<sup>3+</sup> (Fig. 3b) [44]. Furthermore, in Fig. 3c, the peaks at 161.94 eV (S 2p<sub>3/2</sub>) and 163.32 eV (S 2p<sub>1/2</sub>) in ZIS were correspond to S<sup>2-</sup> [11]. In addition, the peaks of Se 3p were observed due to the similar values of S 2p in ZIS/ZnSe. As shown in Fig. 3d, the binding energy of 54.57 eV (Se 3d<sub>5/2</sub>) in ZnSe was attributed to Se<sup>2-</sup> [45]. Furthermore, combining XPS results under dark and light conditions, the electrons transfer of samples was analyzed as follows. As presented in Fig. 3a, in the dark, the binding energies of Zn 2p in ZIS/ZnSe shift to lower energy levels compared with ZnSe. Compared with ZIS, the binding energies of In 3d and S 2p in ZIS/ZnSe shift to higher energy levels in darkness, as shown in Figs. 3b and 3c. In contrast, the binding energy of Se 3d in ZIS/ZnSe was shifted to lower energy levels compared with ZnSe in darkness (in Fig. 3d). According to the analysis of the above changes in binding energies, we observed an increase in the electron density of ZnSe while the decrease in the electron density of ZIS under dark conditions, forming the internal electric field. It indicated that the electrons are transferred from ZIS to ZnSe

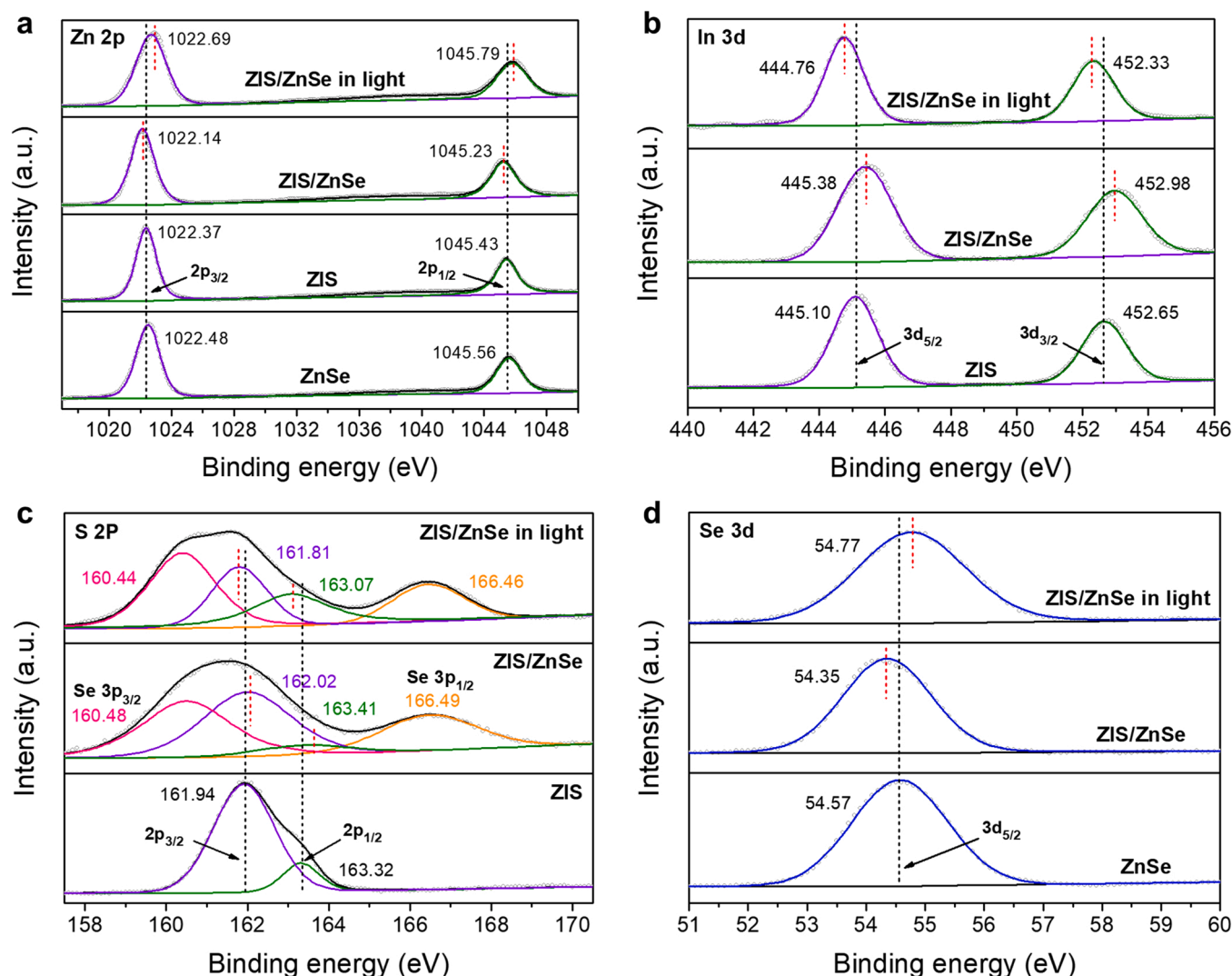


Fig. 3. High-resolution XPS patterns of (a) Zn 2p, (b) In 3d, (c) S 2p, and (d) Se 3d levels of ZnSe NPs, ZIS NSs, and ZIS/ZnSe HNSs, respectively.

[46–48]. However, when in situ XPS measurements are performed, the binding energies of Zn 2p in ZIS/ZnSe have a red shifted under light irradiation (Fig. 3a), compared with the pristine ZnSe. In addition, the binding energies of In 3d and S 2p in ZIS/ZnSe under light irradiation have a blue shifted, compared with ZIS, in Figs. 3b and 3c. Moreover, the binding energy of Se 3d in ZIS/ZnSe was shifted to higher energy levels compared with ZnSe under light irradiation (in Fig. 3d). In conclusion, the electrons could migrate from ZnSe to ZIS under visible light irradiation, which was consistent with our proposed S-scheme mechanism.

In addition, as shown in Fig. S11, compared with ZIS, the binding energies of Zn 2p and S 2p in ZIS/ZnS shift to lower energy levels, indicating an increase in the electron density of ZnS. In contrast, the binding energies of In 3d in ZIS/ZnS shift to higher energy levels compared with ZIS, which implies that the electrons on the conduction band of ZIS are captured by S vacancies in ZnS, forming the electron transfer from ZIS to ZnS [49]. Combined with the above analysis, electron transfer occurs between the composites, which can also be demonstrated by the transient absorption measurements below.

### 3.3. Photocatalytic activity in the HER

The photocatalytic activities of ZIS NSs and ZIS/ZnX (X: S, Se) HNSs in the HER as shown in Fig. 4a, the hydrogen evolution rate of ZIS/ZnSe HNSs was  $1296.9 \mu\text{mol h}^{-1} \text{g}^{-1}$ , which is 2.47 and 6.34 times higher

than that of the ZIS/ZnS HNSs ( $525.2 \mu\text{mol h}^{-1} \text{g}^{-1}$ ) and ZIS NSs ( $204.4 \mu\text{mol h}^{-1} \text{g}^{-1}$ ), respectively, using the  $\text{Na}_2\text{S}-\text{Na}_2\text{SO}_3$  as sacrificial agents under visible-light irradiation ( $\lambda > 420 \text{ nm}$ ). The superior performance in HER of the ZIS/ZnSe HNSs could be attributed to the built-in electric field formed by the interior band gap match, which facilitates the effective separation of photogenerated electron-hole pairs. Compared with the electron trapping in the ZIS/ZnS HNSs for enhancing the photocatalytic activity in HER, the photogenerated electrons of the ZIS/ZnSe HNSs could be more effectively used for water splitting. In addition, we also did the photocatalytic activities in HER of different conditions of the samples. They showed poor performance in HER using the mechanical mixtures and pristine ZnSe and ZnS NPs. It could be concluded that the strong interactions between ZIS phase and ZnSe phase in ZIS/ZnSe HNSs. The stability of photocatalysts is another factor for estimating the photocatalytic properties. The ZIS/ZnSe HNSs still maintained 94% photocatalytic activity after three times recycling (Fig. 4b), and the crystal structure and morphology of the ZIS/ZnSe HNSs were also kept without any significant changes (see Fig. S12 and S13 for details). Furthermore, photocatalytic activities in HER of different amount of ZnSe NPs loading on ZIS NSs, it could be found that the highest photocatalytic activity in HER was achieved when the addition of Se was 0.9 mmol (the ratio of Zn:Se was 2:1 in paper). It indicated that ZnSe in a sunflower structure plays a key role affecting the photo absorption, actives sites and surface reactions. Particularly, the



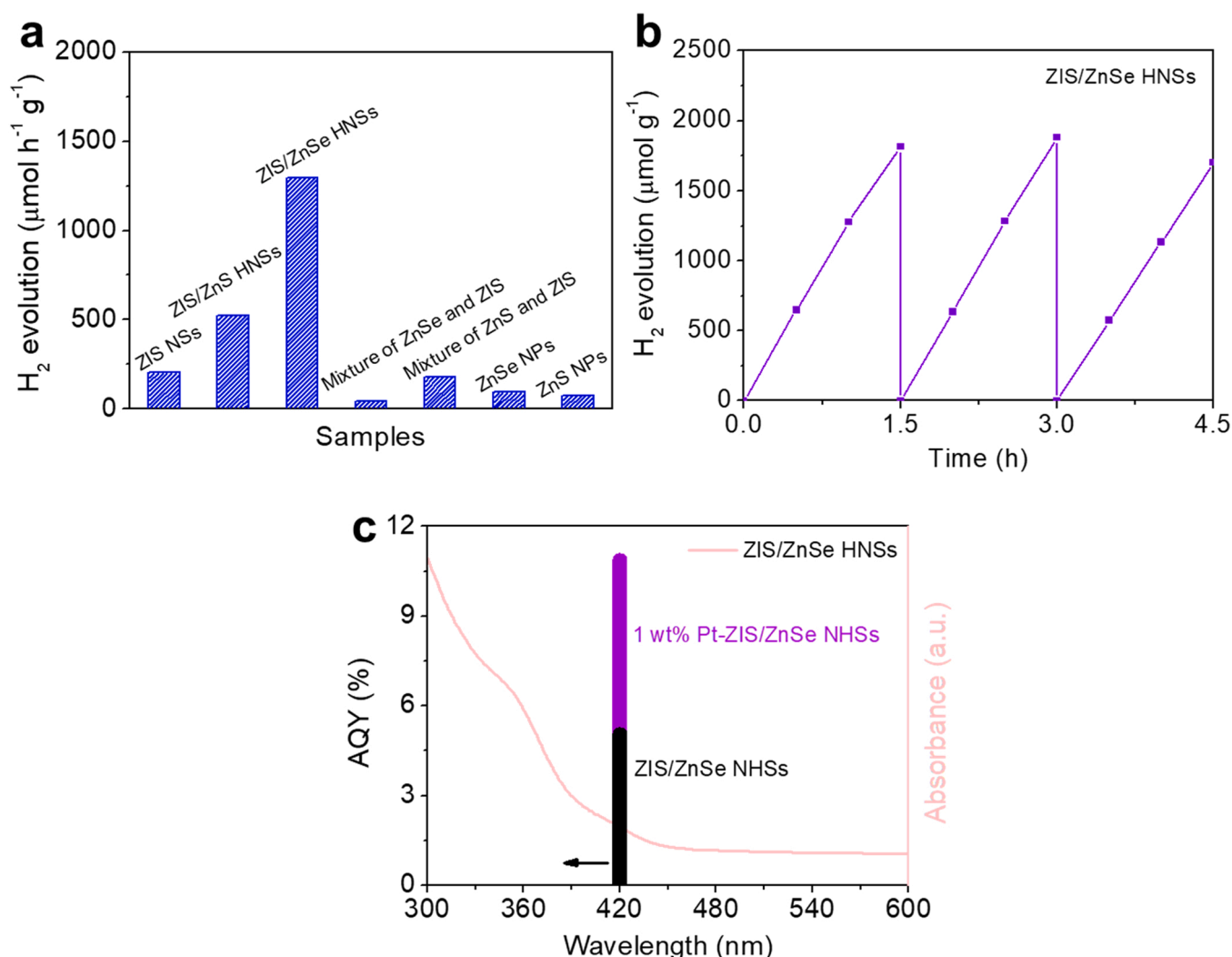


**Fig. 4.** (a) Comparison of H<sub>2</sub> evolution rates for ZIS NSs, ZIS/ZnS HNSs, ZIS/ZnSe HNSs, physical mixtures, and pristine single component under visible-light irradiation ( $\lambda > 420$  nm). The photocatalytic activity of ZnS NPs under visible-light irradiation was attributed to the existence of the defects in ZnS NPs. (b) Recycling testing of ZIS/ZnSe HNSs for the HER under visible light irradiation ( $\lambda > 420$  nm) in the Na<sub>2</sub>S–Na<sub>2</sub>SO<sub>3</sub> aqueous solution as the hole scavengers. (c) AQYs of ZIS/ZnSe HNSs and 1 wt% Pt-ZIS/ZnSe HNSs at 420 nm under identical conditions. The pink line shows the absorption spectrum.

hydrogen production activity ( $3332.2 \mu\text{mol h}^{-1} \text{g}^{-1}$ ) of ZIS/ZnSe HNSs with the loading with 1 wt% platinum (Pt) was increased by 2.57 times, as shown in Fig. S14. In Fig. 4c, the apparent quantum yield (AQY) of the ZIS/ZnSe HNSs was 5.06% at 420 nm. When 1 wt% Pt was photo-deposited on ZIS/ZnSe HNSs, the AQY at 420 nm of the Pt-ZIS/ZnSe HNSs was increased to 10.9%, which was the highest efficiency relative to previous reports (see details in Table S2). These results indicated that the ZnSe and Pt play significant roles in both the photoinduced carrier migration, transportation and surface reaction.

### 3.4. Photoinduced carrier dynamics

To illustrate the photoinduced carrier dynamics supporting the high photocatalytic activity in the HER of the ZIS/ZnSe HNSs, we performed the time-resolved transient absorption (TA) measurements using the femtosecond (fs) pump–probe technique. TA spectra (TAS) of ZIS NSs, ZIS/ZnS HNSs and ZIS/ZnSe HNSs excited by a 300 nm laser were shown in Fig. 5a–c, respectively. We observed exciton photobleaching (XB1 and XB2) by the state-filling of ZIS NSs, and the transition derived from a low energy exciton state to a high energy exciton state (XA1) in Fig. 5a [50,51]. As shown in Fig. 5b, we did not observe the feature of the XB2 in ZIS/ZnS HNSs, which might be attributed to the

photogenerated electron trapping by the S vacancies (Vs) in ZnS phase according to their band diagram. However, the bleaching peak was replaced by the Stokes red-shift of the photoabsorption (XA2) [23]. As shown in Fig. 5c, the appearance of XB3 in ZIS/ZnSe HNSs indicated that the bleaching signal was assigned to the state filling of ZnSe phases. It could be seen that the rapid electron recombination on ZnSe, leading to the emergence of S-scheme, which would be discussed in details below. The weaker XB1 peak in ZIS/ZnSe HNSs indicates that the non-radiative carrier transfer rate in ZIS NSs is reduced after loading ZnSe NPs. Thus, the heterojunction photocatalysts could facilitate the separation of photogenerated electron-hole pairs [52]. Meanwhile, the carrier relaxation to the lowest state results in a rapid decay of the XA2 bands was observed.

To monitor the rate of photoinduced carrier generation and the electron transport rate of the photocatalysts at a 300 nm laser excitation [53], we analyzed the kinetic profiles by the probing light at 370 nm, as shown in Fig. S15. The kinetic trace of the photoinduced excitons bleaching and recovery of ZIS HNSs was also well-fitted by a biexponential function with two components of 2.17 ps ( $\tau_1$ ), 34.0 ps ( $\tau_2$ ), as shown in Table S3. For ZIS/ZnS HNSs, the long lifetime was estimated to be 180 ps, which could be attributed to the electron trapping on the Vs in ZnS phases from conduction band (CB) of ZIS. The defects on the

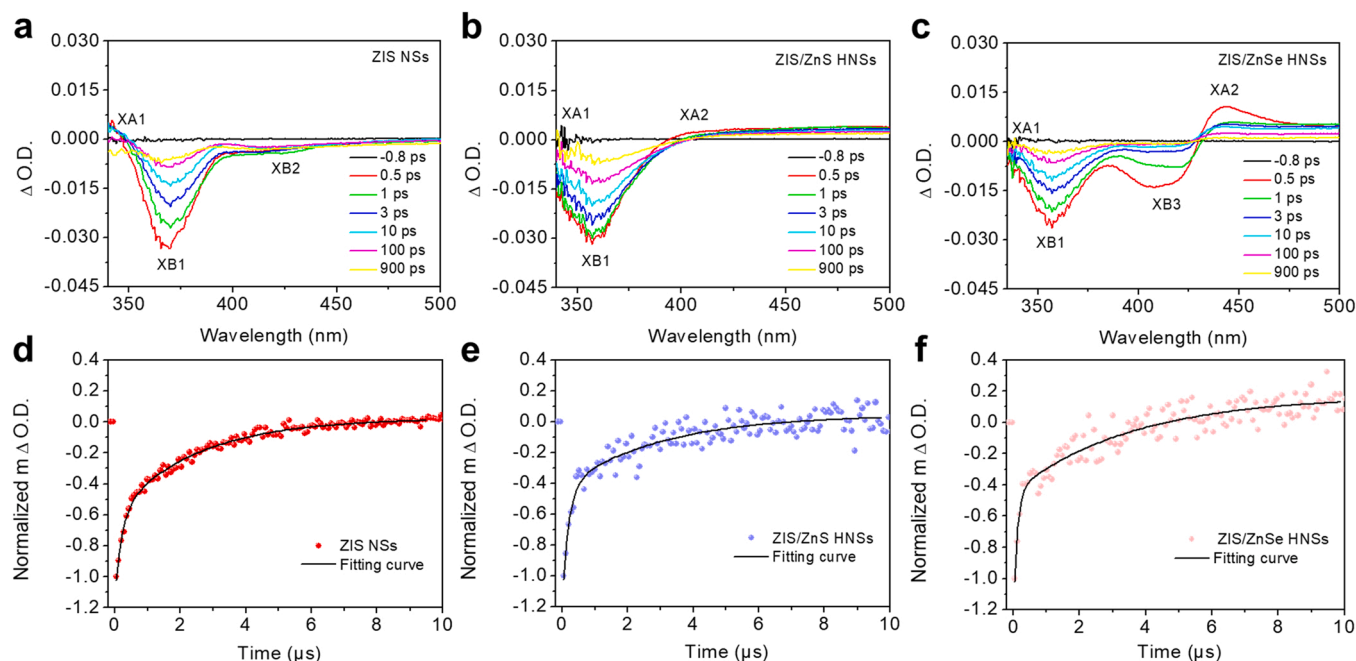


**Fig. 5.** Transient absorption spectra (TAS) of (a) ZIS NSs, (d) ZIS/ZnS HNSs, and (c) ZIS/ZnSe HNSs in the picosecond region upon 300 nm laser excitation. O.D. represents the optical density. Normalized kinetic profile probing at 370 nm for (d) ZIS NSs, (e) ZIS/ZnS HNSs, and (f) ZIS/ZnSe HNSs upon the excitation of a 355 nm laser. The black lines are the best fits for the biexponential functions.

ZIS/ZnS HNSs led to the low photocatalytic activity in HER compared with that of the ZIS/ZnSe HNSs [52]. As comparison in Table S3, the lifetime (38.3 ps) of the ZIS/ZnSe HNSs was much shorter than that of ZIS/ZnS HNSs, indicating that the electrons in the CBs of ZnSe phase could be combined with holes in the valence band (VB) of ZIS NSs forming the S-scheme. It proved that the S-scheme mechanism could use the higher potential of each semiconductor than that of the electron-trap mediated transfer pathway.

Because the recovery of the character of the XB1 feature was not finished within the fs-time window in the TAS, we performed the TA measurements in the microsecond ( $\mu s$ ) region (Fig. 5d-f) upon the excitation of a 355 nm laser. We could clearly observe that the ZIS/ZnSe HNSs have the ultralong lifetime of charge separation at the time constant of 3.58  $\mu s$  compared with that of ZIS and ZIS/ZnS HNSs, as shown in Table S4. It also proved that the S-scheme mechanism in ZIS/ZnSe HNSs achieved the remarkable long-lived charge separation. In addition, to verify the photoinduced electron transfer in ZIS/ZnSe HNSs and ZIS/

ZnS HNSs, we used the anthraquinone dicarboxylic acid (AQ), a typical electron transfer indicator molecule, to trace the dynamics, in which the cation radicals could be monitored probing at 640 nm [54,55]. As shown in Fig. S16, the kinetic profiles of ZIS NSs, ZIS/ZnS HNSs and ZIS/ZnSe HNSs were performed by a 355 nm laser excitation. The second rising component by the biexponential fitting function of ZIS/ZnSe HNSs was estimated to be 0.59  $\mu s$ , which is much longer than that of pristine ZIS NSs and ZIS/ZnS HNSs, as shown in Table S5. It could prove that the electron could be transferred from the samples to AQ molecular, as shown in Fig. S17 and the long lifetime also could support the formation of S-scheme between ZIS and ZnSe that more electron could participate in the HER.

### 3.5. Mechanism for the photocatalytic HER

The photoinduced carrier dynamics in the photocatalytic processes for HER of the ZIS/ZnSe HNSs under visible light irradiation are

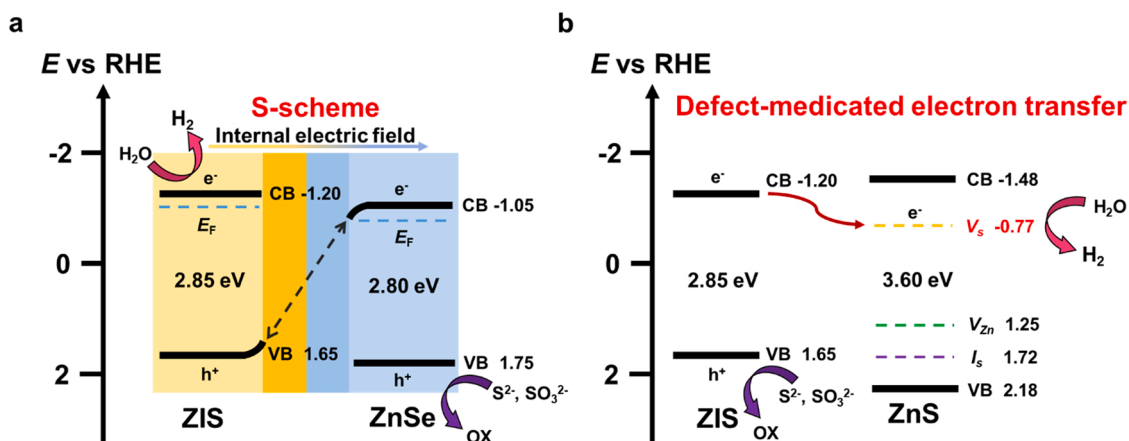


**Fig. 6.** The schematic illustration of the photoinduced carrier dynamics under visible light irradiation. (a) The S-scheme mechanism of ZIS/ZnSe HNSs. (b) The defect-mediated electron trapping mechanism of the ZIS/ZnS HNSs. Optical band gaps of ZIS, ZnSe and ZnS were estimated to be 2.85 eV, 2.80 eV and 3.60 eV, respectively.  $E_F$  are the Fermi levels.  $V_S$ ,  $V_{Zn}$  and  $I_S$  are the S, Zn vacancy sites and S interstitial sites in ZnS, respectively.



displayed in Fig. 6a. Firstly, the ZIS and ZnSe were both excited to produce the electron-hole pairs by visible light. The electron from the CB of ZnSe and the hole from the VB of ZIS could be recombined together, and the CB and Fermi level of ZIS are both more negative than those of ZnSe. The phenomena are the S-scheme mechanism by the formation of internal electric field, which could be efficiently separated the photo-induced carriers. While the electron generated by photoexcitation remained in the more negative CB of ZIS for hydrogen evolution and the hole in VB of ZnSe was consumed by the sacrificial agents [56–58]. As comparison shown in Fig. 6b, the ZIS/ZnS HNSs showed the defect-mediated electron trapping mechanism by the capture of the photogenerated electron of ZIS on S vacancies ( $V_S$ ) in ZnS. It could be suggested that the low chemical potential of the trapped electron reduced the ability of reduction in ZIS/ZnS HNSs, leading to the low photocatalytic activity in HER.

#### 4. Conclusion

In conclusion, we successfully synthesized the ultrathin ZIS/ZnSe HNSs and proposed the formation of the S-scheme mechanism for the photocatalytic activity in HER. The ZIS/ZnSe HNSs achieved the highest photocatalytic activity under visible light irradiation so far than that of the ZIS-based photocatalysts. In addition, TA measurements demonstrated that the superior S-scheme mechanism by the formation of internal electric field in the ZIS/ZnSe HNSs exhibited ultralong lived charge separation (3.58  $\mu$ s) and show the significant advantages over the defect-mediated electron transfer mechanism in ZIS/ZnS HNSs. These results could pave a new route to design the photocatalysts by construction of heterojunctions with the S-scheme mechanism, which could improve their photocatalytic activity and stability.

#### CRedit authorship contribution statement

**Yueqi Zhong:** Formal analysis, Investigation, Data curation, Software, Writing – original draft. **Mengyuan Li:** Investigation, Data curation, Writing – review & editing. **Xue Luan:** Investigation, Data curation, Writing – review & editing. **Fangfang Gao:** Investigation, Data curation, Writing – review & editing. **Hanxiang Wu:** Investigation, Data curation, Writing – review & editing. **Jiangzhi Zi:** Investigation, Data curation, Writing – review & editing. **Zichao Lian:** Conceptualization, Funding acquisition, Writing – review & editing.

#### Declaration of Competing Interest

The authors declare that they have no known competing financial interests or personal relationships that could have appeared to influence the work reported in this paper.

#### Data Availability

Data will be made available on request.

#### Acknowledgments

This work was supported by the National Natural Science Foundation of China (22109097), the Natural Science Foundation of Shanghai (20ZR1472000).

#### Appendix A. Supporting information

Supplementary data associated with this article can be found in the online version at [doi:10.1016/j.apcatb.2023.122859](https://doi.org/10.1016/j.apcatb.2023.122859).

#### References

- [1] Z. Lian, Y. Kobayashi, J.J.M. Vequizo, C.S.K. Ranasinghe, A. Yamakata, T. Nagai, K. Kimoto, K. Kobayashi, K. Tanaka, T. Teranishi, M. Sakamoto, Harnessing infrared solar energy with plasmonic energy upconversion, *Nat. Sustain.* 5 (2022) 1092–1099.
- [2] Z. Lian, Z. Li, F. Wu, Y. Zhong, Y. Liu, W. Wang, J. Zi, W. Yang, Photogenerated hole traps in metal-organic-framework photocatalysts for visible-light-driven hydrogen evolution, *Commun. Chem.* 5 (2022) 93.
- [3] Z. Lian, F. Wu, Y. Zhong, J. Zi, Z. Li, X. Wang, T. Nakagawa, H. Li, M. Sakamoto, Tuning plasmonic p–n junction for efficient infrared-light-responsive hydrogen evolution, *Appl. Catal. B Environ.* 318 (2022), 121860.
- [4] Y. Liu, X. Ye, R. Li, Y. Tao, C. Zhang, Z. Lian, D. Zhang, G. Li, Boosting the photocatalytic nitrogen reduction to ammonia through adsorption-plasmonic synergistic effects, *Chin. Chem. Lett.* 33 (2022) 5162–5168.
- [5] B. Dai, J. Fang, Y. Yu, M. Sun, H. Huang, C. Lu, J. Kou, Y. Zhao, Z. Xu, Construction of infrared-light-responsive photoinduced carriers driver for enhanced photocatalytic hydrogen evolution, *Adv. Mater.* 32 (2020), e1906361.
- [6] Q. Li, Y. Liu, Z. Wan, H. Cao, S. Zhang, Y. Zhou, X. Ye, X. Liu, D. Zhang, Microwave-assisted synthesis of oxygen vacancy associated  $\text{TiO}_2$  for efficient photocatalytic nitrate reduction, *Chin. Chem. Lett.* 33 (2022) 3835–3841.
- [7] Z. Lian, M. Sakamoto, H. Matsunaga, J.J.M. Vequizo, A. Yamakata, M. Haruta, H. Kurata, W. Ota, T. Sato, T. Teranishi, Near infrared light induced plasmonic hot hole transfer at a nano-heterointerface, *Nat. Commun.* 9 (2018) 2314.
- [8] Z. Lian, M. Sakamoto, J.J.M. Vequizo, C.S.K. Ranasinghe, A. Yamakata, T. Nagai, K. Kimoto, Y. Kobayashi, N. Tamai, T. Teranishi, Plasmonic p–n junction for infrared light to chemical energy conversion, *J. Am. Chem. Soc.* 141 (2019) 2446–2450.
- [9] Z. Lian, M. Sakamoto, Y. Kobayashi, N. Tamai, J. Ma, T. Sakurai, S. Seki, T. Nakagawa, M. Lai, M. Haruta, H. Kurata, T. Teranishi, Anomalous photoinduced hole transport in type I core/mesoporous-shell nanocrystals for efficient photocatalytic  $\text{H}_2$  evolution, *ACS Nano* 13 (2019) 8356–8363.
- [10] Z. Lian, M. Sakamoto, Y. Kobayashi, N. Tamai, J. Ma, T. Sakurai, S. Seki, T. Nakagawa, M. Lai, M. Haruta, H. Kurata, T. Teranishi, Dorian-shaped  $\text{CdS}/\text{ZnSe}$  core/mesoporous-shell nanoparticles for enhanced and sustainable photocatalytic hydrogen evolution, *J. Phys. Chem. Lett.* 9 (2018) 2212–2217.
- [11] S. Wang, Y. Wang, S. Zhang, S. Zang, X. Lou, Supporting ultrathin  $\text{ZnIn}_2\text{S}_4$  nanosheets on Co/N-doped graphitic carbon nanocages for efficient photocatalytic  $\text{H}_2$  generation, *Adv. Mater.* 31 (2019), e1903404.
- [12] X. Guo, Y. Peng, G. Liu, G. Xie, Y. Guo, Y. Zhang, J. Yu, An efficient  $\text{ZnIn}_2\text{S}_4/\text{CuInS}_2$  core-shell p–n heterojunction to boost visible-light photocatalytic hydrogen evolution, *J. Phys. Chem. C* 124 (2020) 5934–5943.
- [13] Z. Li, X. Wang, W. Tian, A. Meng, L. Yang, CoNi bimetal cocatalyst modifying a hierarchical  $\text{ZnIn}_2\text{S}_4$  nanosheet-based microsphere noble-metal-free photocatalyst for efficient visible-light-driven photocatalytic hydrogen production, *ACS Sustain. Chem. Eng.* 7 (2019) 20190–20201.
- [14] C. Du, B. Yan, G. Yang, Self-integrated effects of 2D  $\text{ZnIn}_2\text{S}_4$  and amorphous  $\text{Mo}_2\text{C}$  nanoparticles composite for promoting solar hydrogen generation, *Nano Energy* 76 (2020), 105031.
- [15] X. Jiao, Z. Chen, X. Li, Y. Sun, S. Gao, W. Yan, C. Wang, Q. Zhang, Y. Lin, Y. Luo, Y. Xie, Defect-mediated electron-hole separation in one-unit-cell  $\text{ZnIn}_2\text{S}_4$  layers for boosted solar-driven  $\text{CO}_2$  reduction, *J. Am. Chem. Soc.* 139 (2017) 7586–7594.
- [16] M.F. Kuehnel, C.E. Creissen, C.D. Sahm, D. Wielend, A. Schlosser, K.L. Orchard, E. Reisner, ZnSe nanorods as visible-light absorbers for photocatalytic and photoelectrochemical  $\text{H}_2$  evolution in water, *Angew. Chem. Int. Ed.* 58 (2019) 5059–5063.
- [17] M. Kirsanova, A. Nemchinov, N.N. Hewa-Kasakarage, N. Schmall, M. Zamkov, Synthesis of  $\text{ZnSe}/\text{CdS}/\text{ZnSe}$  nanobarels showing photoinduced charge separation, *Chem. Mater.* 21 (2009) 4305–4309.
- [18] C. Yang, J. Wang, R. Wang, W. Zhu, L. Zhang, T. Du, J. Sun, M. Zhu, Y. Shen, J. Wang, Efficient hollow cubic  $\text{Co}_3\text{S}_4/\text{defective ZnS}/\text{g-C}_3\text{N}_4$  for multi-pollutants removal via cascade Z-scheme heterojunction, *Appl. Catal. B Environ.* 322 (2023), 122084.
- [19] X. Tao, Y. Gao, S. Wang, X. Wang, Y. Liu, Y. Zhao, F. Fan, M. Dupuis, R. Li, C. Li, Interfacial charge modulation: an efficient strategy for boosting spatial charge separation on semiconductor photocatalysts, *Adv. Energy Mater.* 9 (2019), 1803951.
- [20] Y. Guo, W. Shi, Y. Zhu, Internal electric field engineering for steering photogenerated charge separation and enhancing photoactivity, *EcoMat* 1 (2019), e12007.
- [21] L. Zhang, J. Zhang, H. Yu, J. Yu, Emerging S-scheme photocatalyst, *Adv. Mater.* 34 (2022), 2107668.
- [22] Y. Zhong, J. Zi, F. Wu, Z. Li, X. Luan, F. Gao, Z. Lian, Defect-mediated electron transfer in Pt-CuInS<sub>2</sub>/CdS heterostructured nanocrystals for enhanced photocatalytic  $\text{H}_2$  evolution, *ACS Appl. Nano Mater.* 5 (2022) 7704–7713.
- [23] J. Zi, Y. Zhong, Z. Li, F. Wu, W. Yang, Z. Lian, Type-I CdSe/ZnS heteronanostructures exhibit enhanced photocatalytic hydrogen evolution by interfacial trap-mediated hole transfer, *J. Phys. Chem. C* 125 (2021) 23945–23951.
- [24] S. Luo, J. Ke, M. Yuan, Q. Zhang, P. Xie, L. Deng, S. Wang, CuInS<sub>2</sub> quantum dots embedded in  $\text{Bi}_2\text{WO}_6$  nanoflowers for enhanced visible light photocatalytic removal of contaminants, *Appl. Catal. B Environ.* 221 (2018) 215–222.
- [25] Y. Zou, J. Shi, L. Sun, D. Ma, S. Mao, Y. Lv, Y. Cheng, Energy-band-controlled  $\text{Zn}_x\text{Cd}_{1-x}\text{In}_2\text{S}_4$  solid solution coupled with g-C<sub>3</sub>N<sub>4</sub> nanosheets as 2D/2D heterostructure toward efficient photocatalytic  $\text{H}_2$  evolution, *Chem. Eng. J.* 378 (2019), 122192.

- [26] Y. Choi, M. Beak, K. Yong, Solar-driven hydrogen evolution using a CuInS<sub>2</sub>/CdS/ZnO heterostructure nanowire array as an efficient photoanode, *Nanoscale* 6 (2014) 8914–8918.
- [27] J. Ran, B. Zhu, S. Qiao, Phosphorene co-catalyst advancing highly efficient visible-light photocatalytic hydrogen production, *Angew. Chem. Int. Ed.* 56 (2017) 10373–10377.
- [28] C. Hao, W. Wang, R. Zhang, B. Zou, H. Shi, Enhanced photoelectrochemical water splitting with TiO<sub>2</sub>@Ag<sub>2</sub>O nanowire arrays via p-n heterojunction formation, *Sol. Energy Mater. Sol. Cells* 174 (2018) 132–139.
- [29] J. Shi, Y. Zou, L. Cheng, D. Ma, D. Sun, S. Mao, L. Sun, C. He, Z. Wang, In-situ phosphating to synthesize Ni<sub>2</sub>P decorated NiO/g-C<sub>3</sub>N<sub>4</sub> p-n junction for enhanced photocatalytic hydrogen production, *Chem. Eng. J.* 378 (2019), 122161.
- [30] H. Huang, K. Xiao, Y. He, T. Zhang, F. Dong, X. Du, Y. Zhang, In situ assembly of BiOI/Bi<sub>12</sub>O<sub>7</sub>Cl<sub>2</sub> p-n junction: charge induced unique front-lateral surfaces coupling heterostructure with high exposure of BiOI {001} active facets for robust and nonselective photocatalysis, *Appl. Catal. B Environ.* 199 (2016) 75–86.
- [31] X. Hao, Y. Wang, J. Zhou, Z. Cui, Y. Wang, Z. Zou, Zinc vacancy-promoted photocatalytic activity and photostability of ZnS for efficient visible-light-driven hydrogen evolution, *Appl. Catal. B Environ.* 221 (2018) 302–311.
- [32] X. Chu, X. Wang, J. Li, D. Yao, X. Fang, F. Fang, Z. Wei, X. Wang, Influence factors and mechanism of emission of ZnS:Cu nanocrystals, *Chin. Phys. B* 24 (2015), 067805.
- [33] Y. Lin, Q. Zhang, Y. Li, Y. Liu, K. Xu, J. Huang, X. Zhou, F. Peng, The evolution from a typical Type-I CdS/ZnS to Type-II and Z-scheme hybrid structure for efficient and stable hydrogen production under visible light, *ACS Sustain. Chem. Eng.* 8 (2020) 4537–4546.
- [34] Y. Zhi, Y. Yi, C. Deng, Q. Zhang, S. Yang, F. Peng, Defect-enriched ZnO/ZnS heterostructures derived from hydrozincite intermediates for hydrogen evolution under visible light, *ChemSusChem* 15 (2022), e202200860.
- [35] T. Chen, B. Liu, M. Li, L. Zhou, D. Lin, X. Ding, J. Lian, J. Li, R. He, T. Duan, W. Zhu, Efficient uranium reduction of bacterial cellulose-MoS<sub>2</sub> heterojunction via the synergistically effect of Schottky junction and S-vacancies engineering, *Chem. Eng. J.* 406 (2021), 126791.
- [36] Q. Gao, W. Luo, X. Ma, Z. Ma, S. Li, F. Gou, W. Shen, Y. Jiang, R. He, M. Li, Electronic modulation and vacancy engineering of Ni<sub>3</sub>S<sub>2</sub> to synergistically boost efficient water splitting: active vacancy-metal pairs, *Appl. Catal. B Environ.* 310 (2022), 121356.
- [37] Z. Lian, Y. Tao, Y. Liu, Y. Zhang, Q. Zhu, G. Li, H. Li, Efficient self-driving photoelectrocatalytic reactor for synergistic water purification and H<sub>2</sub> evolution, *ACS Appl. Mater. Interfaces* 12 (2020) 44731–44742.
- [38] P. Zhang, Y. Li, Y. Zhang, R. Hou, X. Zhang, C. Xue, S. Wang, B. Zhu, N. Li, G. Shao, Photogenerated electron transfer process in heterojunctions: in situ irradiation XPS, *Small Methods* 4 (2020), 2000214.
- [39] J. Low, B. Dai, T. Tong, C. Jiang, J. Yu, In situ irradiated X-ray photoelectron spectroscopy investigation on a direct Z-scheme TiO<sub>2</sub>/CdS composite film photocatalyst, *Adv. Mater.* 31 (2019), e1802981.
- [40] C.R. O'Connor, M.A. van Spronsen, M. Karatok, J. Boscoboinik, C.M. Friend, M. M. Montemore, Predicting X-ray photoelectron peak shapes: The effect of electronic structure, *J. Phys. Chem. C* 125 (2021) 10685–10692.
- [41] J. Liu, M. Wu, H. Ye, Y. Xie, Y. Ma, L. Liu, Strong interaction between sulfur sites and oxygen vacancies in Z-scheme ZnIn<sub>2</sub>S<sub>4</sub>/TiO<sub>2-x</sub> heterojunction for improved photocatalytic hydrogen yield and stability, *Chem. Eng. J.* 455 (2023), 140722.
- [42] L. Li, D. Ma, Q. Xu, S. Huang, Constructing hierarchical ZnIn<sub>2</sub>S<sub>4</sub>/g-C<sub>3</sub>N<sub>4</sub> S-scheme heterojunction for boosted CO<sub>2</sub> photoreduction performance, *Chem. Eng. J.* 437 (2022), 135153.
- [43] S. Wang, B. Guan, X. Lou, Construction of ZnIn<sub>2</sub>S<sub>4</sub>-In<sub>2</sub>O<sub>3</sub> hierarchical tubular heterostructures for efficient CO<sub>2</sub> photoreduction, *J. Am. Chem. Soc.* 140 (2018) 5037–5040.
- [44] Y. Xia, B. Cheng, J. Fan, J. Yu, G. Liu, Near-infrared absorbing 2D/3D ZnIn<sub>2</sub>S<sub>4</sub>/N-doped graphene photocatalyst for highly efficient CO<sub>2</sub> capture and photocatalytic reduction, *Sci. China Mater.* 63 (2020) 552–565.
- [45] R. Zeng, C. Cheng, F. Xing, Y. Zou, K. Ding, C. Huang, Dual vacancies induced local polarization electric field for high-performance photocatalytic H<sub>2</sub> production, *Appl. Catal. B Environ.* 316 (2022), 121680.
- [46] J. Fu, Q. Xu, J. Low, C. Jiang, J. Yu, Ultrathin 2D/2D WO<sub>3</sub>/g-C<sub>3</sub>N<sub>4</sub> step-scheme H<sub>2</sub>-production photocatalyst, *Appl. Catal. B Environ.* 243 (2019) 556–565.
- [47] F. He, B. Zhu, B. Cheng, J. Yu, W. Ho, W. Macyk, 2D/2D/0D TiO<sub>2</sub>/C<sub>3</sub>N<sub>4</sub>/Ti<sub>3</sub>C<sub>2</sub> MXene composite S-scheme photocatalyst with enhanced CO<sub>2</sub> reduction activity, *Appl. Catal. B Environ.* 272 (2020), 119006.
- [48] H. Ge, F. Xu, B. Cheng, J. Yu, W. Ho, S-scheme heterojunction TiO<sub>2</sub>/CdS nanocomposite nanofiber as H<sub>2</sub>-production photocatalyst, *ChemCatChem* 11 (2019) 6301–6309.
- [49] L. Qiu, Y. Wang, X. Zhang, F. Tian, C. Zhu, J. Sheng, W. Yang, Y. Yu, ZnS nanospheres coated with ZnSe/MoSe<sub>2</sub> shells as dual heterojunctions with wide spectral responses for the photoreduction of Cr(VI), *ACS Appl. Nano Mater.* 6 (2023) 523–532.
- [50] P. Tyagi, P. Kambhampati, False multiple exciton recombination and multiple exciton generation signals in semiconductor quantum dots arise from surface charge trapping, *J. Chem. Phys.* 134 (2011), 094706.
- [51] H. Bhatt, T. Goswami, D.K. Yadav, N. Ghorai, A. Shukla, G. Kaur, A. Kaur, H. N. Ghosh, Ultrafast hot electron transfer and trap-state mediated charge carrier separation toward enhanced photocatalytic activity in g-C<sub>3</sub>N<sub>4</sub>/ZnIn<sub>2</sub>S<sub>4</sub> heterostructure, *J. Phys. Chem. Lett.* 12 (2021) 11865–11872.
- [52] T. Goswami, D.K. Yadav, H. Bhatt, G. Kaur, A. Shukla, K.J. Babu, H.N. Ghosh, Defect-mediated slow carrier recombination and broad photoluminescence in non-metal-doped ZnIn<sub>2</sub>S<sub>4</sub> nanosheets for enhanced photocatalytic activity, *J. Phys. Chem. Lett.* 12 (2021) 5000–5008.
- [53] X. Lin, Z. Chen, Y. Han, C. Nie, P. Xia, S. He, J. Li, K. Wu, ZnSe/ZnS core/shell quantum dots as triplet sensitizers toward visible-to-ultraviolet B photon upconversion, *ACS Energy Lett.* 7 (2022) 914–919.
- [54] S.A. Carlson, D.M. Hercules, Studies on some intermediates and products of the photoreduction of 9,10-anthraquinone, *Photochem. Photobiol.* 17 (1973) 123–131.
- [55] H. Zhu, Y. Yang, K. Hyeon-Deuk, M. Califano, N. Song, Y. Wang, W. Zhang, O. V. Prezhdo, T. Lian, Auger-assisted electron transfer from photoexcited semiconductor quantum dots, *Nano Lett.* 14 (2014) 1263–1269.
- [56] Y. Xi, W. Chen, W. Dong, Z. Fan, K. Wang, Y. Shen, G. Tu, S. Zhong, S. Bai, Engineering an interfacial facet of S-scheme heterojunction for improved photocatalytic hydrogen evolution by modulating the internal electric field, *ACS Appl. Mater. Interfaces* 13 (2021) 39491–39500.
- [57] Q. Xu, L. Zhang, B. Cheng, J. Fan, J. Yu, S-scheme heterojunction photocatalyst, *Chem* 6 (2020) 1543–1559.
- [58] S. Gong, X. Teng, Y. Niu, X. Liu, M. Xu, C. Xu, L. Ji, Z. Chen, Construction of S-scheme 0D/2D heterostructures for enhanced visible-light-driven CO<sub>2</sub> reduction, *Appl. Catal. B Environ.* 298 (2021), 120521.